# Micromechanical origins of remarkable elongation-to-fracture in AHSS TRIP steels via continuous bending under tension

Rishabh Sharma[1], Camille M. Poulin[2], Marko Knezevic[2], Michael P. Miles[3], David T. Fullwood[1]

[1]Department of Mechanical Engineering, Brigham Young University, Utah, USA

[2] Mechanical Engineering Department, University of New Hampshire, New Hampshire, USA

[3] Manufacturing Engineering Department, Brigham Young University, Utah, USA

## Abstract

Continuous bending under tension (CBT) is known to achieve elongation-to-failure well above that achieved under a conventional uniaxial simple tension (ST) strain path. However, the detailed mechanism for supplying this increased ductility has not been fully understood. It is clear that the necking that occurs in a typical ST specimen is avoided by constantly moving the region of plastic deformation during the CBT process. The volume of material in which the flow stress is greatest is limited to a moving line where the rollers contact the sheet and superimpose bending stress on the applied tensile load. Hence the condition of a large volume of material experiencing stress greater than the material flow stress, leading to strain localization during ST, is avoided. However, the magnitude of the contribution of this phenomenon to the overall increase in elongation is unclear. In the current set of experiments, an elongation to fracture (ETF) of 4.56x and 3.7x higher than ST was achieved by fine-tuning CBT forming parameters for Q&P 1180 and TBF 1180, respectively. A comparison of maximum local strains near the final point of fracture in ST and CBT sheets via digital image correlation revealed that avoidance of localization of plastic strain during CBT accounts for less than half of the increased elongation in the CBT specimens for two steels containing different amounts of retained austenite (RA). Geometrically necessary dislocation evolution is monitored using high-resolution EBSD (HREBSD) for both strain paths, indicating a lower hardening rate in the CBT samples in the bulk of the sheet, potentially relating to the cyclical nature of the stress in the outer layers of the sheet. Interestingly, the GND evolution in the center of the sheet, which does not experience the same amplitude of cyclic stress, follows the ST behavior more closely than the sheet edges. This appears to contribute to a precipitous drop in residual ductility for the specimens that are pulled in ST after partial CBT processing. The rate of transformation of RA is also tracked in the steels, with a significantly lower rate of transformation during CBT, compared to ST. This suggests that a slower transformation rate achieved under CBT also contributed to higher strain-to-failure levels.

**Keywords:** Dislocations, Ductility, Phase transformation, Electron Microscopy, Digital Image Correlation.

## Introduction

In recent years, much attention has been focused on understanding the relationships between microstructure and deformation response of high-strength steels in order to improve their formability, and thus contribute to lighter vehicle structures that meet the need for reduced energy consumption in transportation (Bhargava et al., 2018; Hirsch and Al-Samman, 2013; Ma et al., 2016; Yaddanapudi et al., 2021). One resultant strategy involves the development of microstructures with complex phase compositions, to find a delicate compromise between strength and ductility. Transformation-induced plasticity (TRIP) - assisted steels are composed of varying fractions of ferrite, martensite, bainite, and retained austenite (RA) phases. The proportions and morphologies of the various phases determine the strength and ductility as well as the elastic properties of the particular alloy (Cantara et al., 2019; Eghtesad and Knezevic, 2020; Zecevic et al., 2016a). The ferrite, being a softer phase, delivers ductility to the alloy while the harder phases provide strength. During the heat treatments of TRIP-assisted steels, a fraction of the original austenite can be stabilized by diffusing extra carbon from surrounding high-carbon concentration martensite (Billur and Altan, 2013). On applying plastic strain to the resultant alloy, the RA transforms into martensite to accommodate strain, thus contributing to the overall plastic response (Fischer et al., 2000; Ma and Hartmaier, 2015; Matlock and Speer, 2010; Tamura, 1982; Tirumalasetty et al., 2012b). The excellent combination of strength and ductility of these alloys is essential in automotive applications for reducing a vehicle's weight while maintaining/improving crashworthiness.

A complementary area of study, for enabling low-cost (e.g., room temperature) forming, focuses on designing and understanding novel forming techniques. For example, enhanced formability has been reported for shear, bending, and nonplanar stress (Emmens and van den Boogaard, 2009c). Incremental sheet forming (ISF) processes can achieve strains well above those identified on the forming limit curve (FLC), which are typically obtained through proportional strain paths. Continuous bending under tension (CBT) is an ISF tool that has been shown to dramatically delay necking and failure in metals by superimposing a bending load on a tensile load. The resultant deformation in the sheet primarily results from bending. The deformation mode at the sheet surfaces alternates between tension and compression, thus introducing a Bauschinger effect which further reduces the required tensile load for plastic deformation (Sanchez, 2010; Yoshida et al., 2015; Zecevic et al., 2017). The loading strategy results in a through-thickness stress gradient across the sheet (Emmens and van den Boogaard, 2011). The outermost zones undergo the mentioned reverse loading from maximum tension to compression as they pass over the alternating rollers, resulting in a ratcheting (cyclic tension-compression) effect in the force-displacement curve. However, the middle zone stays under monotonic tension throughout the process. The size of the middle zone can be controlled by changing the process parameters, such as crosshead velocity and roller diameter and depth. The tensile load on one side of the sheet locally plastically deforms a moving line of the material as the sheet passes over the rollers (Emmens and van den Boogaard, 2009a). Eventually, the width of the ratcheting zones is diminished with a reduction in sheet thickness and a shifting of the neutral axis outside the sheet, putting the whole sheet in uniaxial tension and causing a failure similar to that seen in ST (Emmens and van den Boogaard, 2009a).

Impressive improvements in elongation-to-fracture (ETF) under optimum CBT forming conditions, when compared with simple tension (ST) deformation, have been reported in various studies. A study by Emmens et al. found that under optimum CBT forming conditions, the ETF for an AISI 1006 steel can be increased from 22% to 290% (Nikhare et al., 2012). Zecevic et al. developed a custom experimental apparatus. The setup in the study had a set of fixed rollers instead of moving ones to more easily monitor sheet behavior with respect to the roller position (Roemer et al., 2015; Zecevic et al., 2016b). In an initial test with aluminum 6022-T4 alloy, an increase in ETF from 24% to 52% was reported. Poulin et al. performed experiments on DP1180 using the same equipment and observed an increase in ETF from 13% to 47% p(Poulin et al., 2020; Poulin et al., 2019).

While there has been discussion about the cause of the increased elongation (as briefly mentioned), there has been no detailed study of the relative contributions from the various mechanisms that contribute to the extraordinary increase in elongation. Macroscopically, a large increase in ductility under CBT has been associated with incremental sheet forming underneath the rollers avoiding a large volume of uniform plastic deformation that leads to necking and failure. The current work builds upon two recent studies that investigated the effect of strain path on RA transformation rate and ductility in Quenched and Partitioned (Q&P) 1180 and Trip-assisted bainitic ferritic (TBF) 1180 advanced high strength steels (AHSS). These alloys demonstrated reasonable formability for various proportional strain paths, especially considering their high levels of strength (Cramer et al., 2018; Gibbs, 2019). The current study aims to significantly increase the formability of these advanced high strength steels via CBT, in order to gain an understanding of the underlying micromechanical deformation mechanisms and thereby translate this enhanced performance to an industrial forming process, like automotive stamping.

The deformation response of these alloys was studied while varying two main CBT parameters: normalized roller bending depth and crosshead velocity. Digital image correlation (DIC) was employed to accurately map the surface strains of the sheet specimens during CBT forming. Deformation behavior was then correlated to the microstructure evolution at varying plastic strains using combined electron backscatter diffraction (EBSD) and high-resolution EBSD (HR-EBSD) techniques to observe phase and dislocation evolution.

## Experimental Procedures

The composition of the two steels is given in Table 1. The 1.2 mm thick Q&P 1180 and 1 mm thick TBF 1180 sheets were procured from General Motors. Prior to CBT experiments, the deformation behavior of both materials was assessed under uniaxial simple tension (ST). The elongation-to-failure resulting from ST was used as a reference to evaluate the improvement in the ETF under CBT conditions. The tensile specimens were machined along the 0° and 90° orientations with respect to the rolling direction (RD) of the sheet, according to the dimensions shown in Figure 1. The geometry follows the ASTM E8 specimen configuration, with an extended gauge section to accommodate the CBT roller motion and maintain a significant gauge length that passed through all three rollers on each cycle. For ST, the specimens were pulled at 0.001 $s^{-1}$ initial strain rate and force-strain data was recorded using a combination of load-cell and extensometer. The specimens' thickness and width were recorded at five different points along the gauge length

to accurately calculate the applied true stress, which was plotted against the true strain data from the extensometer.

*Table 1 Chemical composition of Q&P and TRIP 1180. (wt%)*

| Steel | C | Si | Mn |
|---|---|---|---|
| **TBF 1180** | 0.2 | 1.5 | 1.5-2.5 |
| **Q&P 1180** | 0.2 | 1.0-2.0 | 1.5-3.0 |

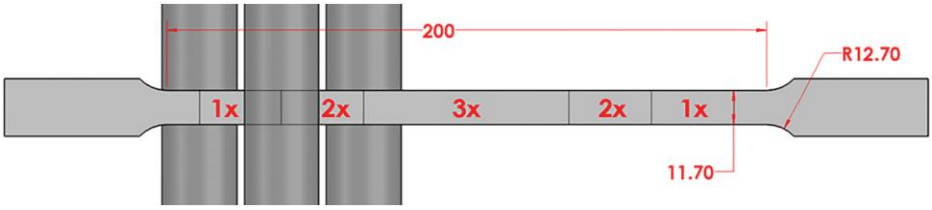


*Figure 1 CBT specimen and dimensions in millimeters with strain zones shown on the specimen (1x, 2x, and 3x not to scale) (Poulin et al., 2019).*

Tensile testing machines equipped with a set of rollers moving up and down have been typically used for CBT (Emmens and van den Boogaard, 2009b). However, greater control of the process is available from a machine specialized for CBT processing (Zecevic et al., 2016b). This machine is utilized for the present study (Figure 2b). In this design, the three main components include: (1) a moving carriage holding a specimen and the axial loading system, (2) a stationary roller assembly mounted on the machine base, and (3) a data acquisition and control software/hardware. The carriage reciprocates during the CBT test with a certain velocity. The rollers are of diameter, D = 25.4 mm, providing a strain in bending of 0.038 for a sheet of t = 1 mm if the wrapping is perfect. Thicker sheets experience a slightly larger strain. However, in practice, the wrapping is not perfect for typical bending depths used in CBT processing. The bottom rollers are L = 54 mm apart, while the top roller is vertically adjustable providing a possibility to set a bending depth, $\delta$ as shown in Figure 2a. The machine has two donut-style Futek load cells, LCF 450 (capacity of 22.24 kN) attached to the carriage and LTH 500 (capacity of 22.24 kN) attached to the actuator. The hydraulic actuator supplying crosshead (pulling) velocity has a Balluff Micropulse BTL7-A501-M0305-Z-S32 position sensor with a resolution of 5 µm. The carriage motion is determined by a pair of limit switches, one positioned on the grip attached to the hydraulic cylinder and another positioned on the base. Limit switches signal the end of the stroke and change in direction for the moving carriage. More details in terms of the machine design can be found in (Barrett et al., 2020; Roemer et al., 2019).

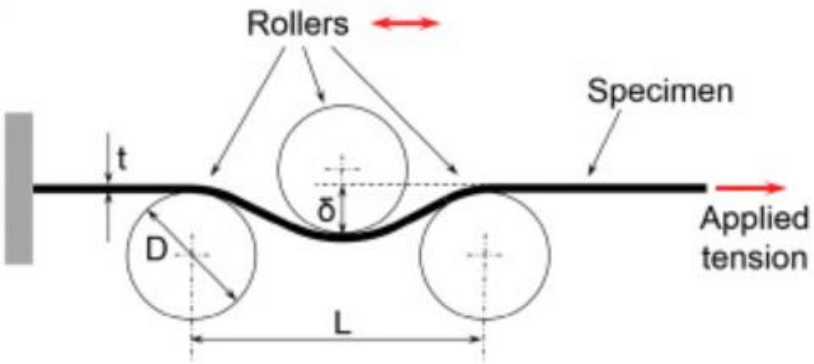


*Figure 2a Schematic of continuous-bending under tension testing apparatus (Poulin et al., 2019).*

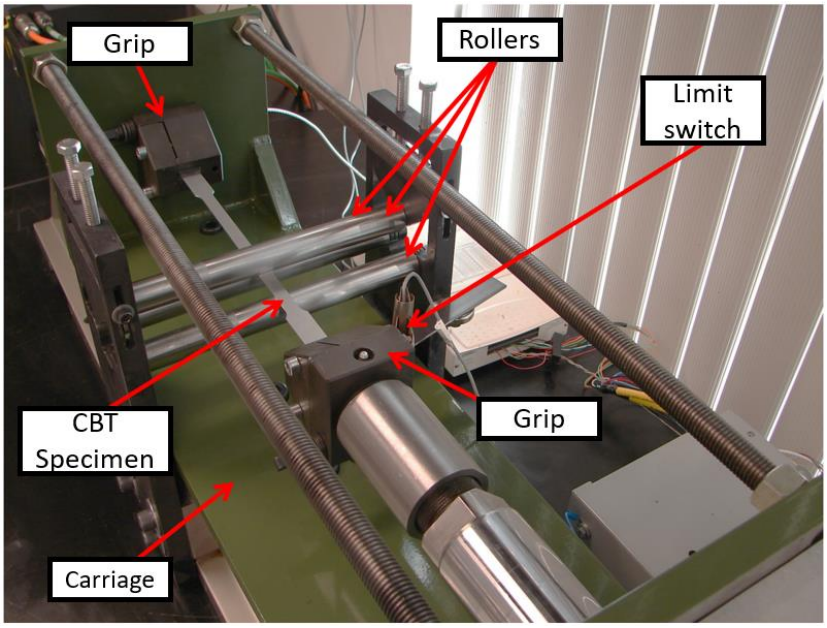


*Figure 2b A photo depicting the main components of the CBT testing machine.*

Unlike ST, where the applied stress and resultant strain are initially uniform along the entire gauge length, the CBT method applies a complex and varying stress state that results in a local strain level correlating with the number of times a roller has passed over a given point. Hence, there are seven regions along the ST gauge length that represent different levels of strain, depending upon whether rollers pass the location 0, 1, 2, or 3 times on each pass (the 1x, 2x, and 3x regions are highlighted in Figure 1). The gauge length for CBT should therefore be taken to be the length of the 3x region, which undergoes an approximately consistent level of strain.

A 2D full-field strain profile of the normal direction (ND) surface was obtained by digital image correlation (DIC). A speckle pattern was applied to the region of interest using a polymer-based black and white paint. A 12.2-megapixel camera with f/1.8 aperture and phase-detection autofocus was used to capture high contrast images at 96 PPI resolution (Figure 3), with the specimen surface illuminated by a secondary LED light. The trigger was controlled manually to capture a point in time at the end of each CBT stroke. The captured images were processed using

open-source MatLab (2014) based DIC software NCorr (Blaber, 2014). Developed at the Georgia Institute of Technology, previous studies have found that results obtained from NCorr were in good agreement with other commercial alternatives (Blaber et al., 2015; Harilal, 2014; Scalici et al., 2015). The images were processed for the ND surfaces along the gauge length to identify and map the strain.

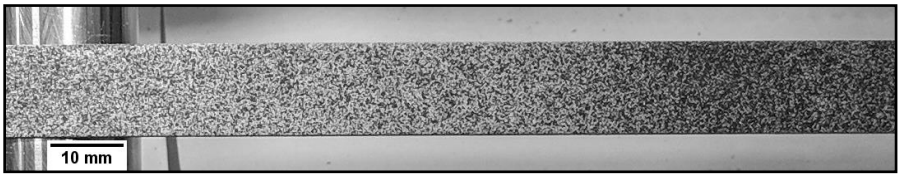


*Figure 3 Image of polymer-speckle pattern on the CBT specimen ND surface.*

Both the ST and CBT processes were interrupted at specified intervals (defined by a number of cycles for the CBT tests) to remove microscopy samples from the highest strain region of the specimens (3x strain region in the case of CBT). The samples were removed using a diamond blade cutter, to avoid further deformation of the material, and mounted in epoxy resin to polish for EBSD scanning. The ND surface of the samples was first ground with grits of 400, 600, 800, 1200, and 1200 fine abrasive paper. The ground samples were then electropolished using an electrolyte solution of 25 ml perchloric acid, 75 ml butanol, and 125 ml methanol under 20 volts and 2 amps at 10°C for 20 secs. The polished surface of the samples was indexed using EDAX OIM software (2010) for ferrite (BCC) and retained austenite (FCC) phases; other constituent phases such as martensite and bainite would show up as ferrite in the EBSD images.

In conjunction with the RA analysis, the interrupted samples were also mapped for geometrically necessary dislocations (GNDs). In a polycrystalline material, dislocation motion is the principal mechanism for plastic deformation (Ahmed and Hartmaier, 2010); as these dislocations interact, the dislocation density in the material increases, resulting in strain hardening. Eventually, the dislocation density saturates, leading to strain localization, due to plastic instability, and subsequent failure (Antolovich and Armstrong, 2014; Weng, 1990). While EBSD methods cannot directly measure total dislocation density, the rate of accumulation of GNDs is likely to correlate with total dislocation density, and thereby indicate the level of strain hardening in the sample. In this study, the HR-EBSD technique was employed to calculate the GND density in undeformed and deformed specimens, using OpenXY (BYU, 2015). Three different areas of 400 sq. microns with 80 nm step size, from each electropolished sample, were used to plot GND with error bars for every strain percent. The GND calculations are based on the dislocation density tensor (α) introduced by Nye (Ruggles and Fullwood, 2013):

$$\rho \approx \frac{1}{b}\|\alpha\|_1 \, , \alpha = \nabla \times \beta \quad (1)$$

where ρ is dislocation density, b is the average Burger's vector, $\beta$ is the elastic distortion as measured by HREBSD, and $\|\alpha\|_1$ is the $L_1$ norm on a tensor. The average GND density in the material was determined after filtering the data for "bad" scan points with low CI (Cramer et al., 2018).

Finally, smaller tensile specimens were cut from the 3x region of the interrupted CBT specimens in order to determine the residual ductility after CBT processing. These extracted specimens were tested under ST in the same way as described for the un-processed material.

## Results

This section presents baseline simple tension data for the two steels of interest. Optimal CBT parameters are then established, before comparing the CBT and ST values of ETF and Load/Original area vs strain (shown later). The homogeneity of strain experienced across the CBT samples is examined using DIC, along with the evolution of GNDs and RA during deformation. Finally, the residual ductility (as measured by an ST test) is examined for CBT specimens that have been strained to various levels. The insights gleaned from these results are discussed in a subsequent section.

Simple tension tests were performed on both steels in both the RD and transverse directions (TD). Q&P steel exhibits a sharper transition from elastic to plastic deformation, and a more stable hardening rate, compared with TBF (Figure 4). Only small differences in deformation response were observed between the two directions, for both steels. Hence, all CBT tests were performed with the specimen in a single orientation, that of RD.

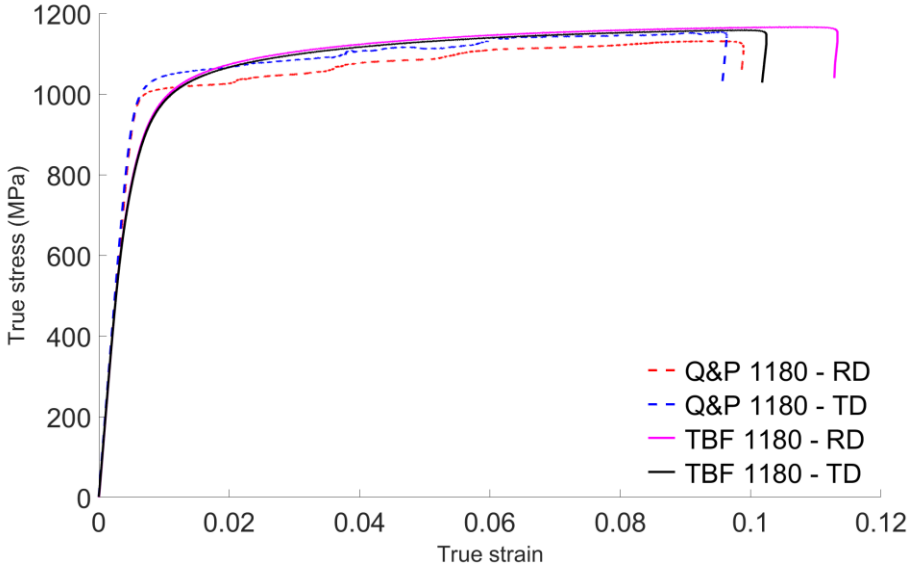


*Figure 4 True ST stress-strain curves at 0.001 s-1 strain rate for Q&P and TBF 1180 steels in RD and TD direction.*

The CBT parametric space was sampled for the two steels to find approximately optimal CBT parameters, guided by a previous study on DP 1180 (Poulin et al., 2019). The velocity at which rollers traverse the specimen, i.e., the carriage velocity, was kept constant at 66 mm/s which is the maximum the setup could achieve. Tests on DP 1180 steel from the Poulin et al. study indicated low sensitivity to variation of this parameter. The crosshead velocity (υ) and normalized bending depth with sheet thickness (δ/t) were both varied over a small set of values. The Poulin study indicated that the optimal crosshead velocity would be in the range between 1.25 mm/s and 1.35

mm/s; hence these values were selected for the current tests. The bending depth was normalized to incorporate any dependency on the sheet thickness (Poulin et al., 2019); the appropriateness of the normalization is analyzed in the discussion section. The initial normalized bend depth for the Q&P and TBF 1180 trials was once again guided by the prior DP 1180 results. An initial value of 2.75 was selected for the Q&P steel, and the depth increased until an optimal ETF value was reached. The same approach was taken for the TBF 1180 steel, beginning with the optimal value of 3 that was identified from the Q&P 1180 tests. Force-displacement data for all tests is shown in Figure 5 and summarized in Table 2. The close-to-optimum CBT parameter combinations for Q&P and TBF occurred at $\delta/t = 3$ and 3.5, respectively, and with values of $\upsilon = 1.35$ mm/s for both steels.

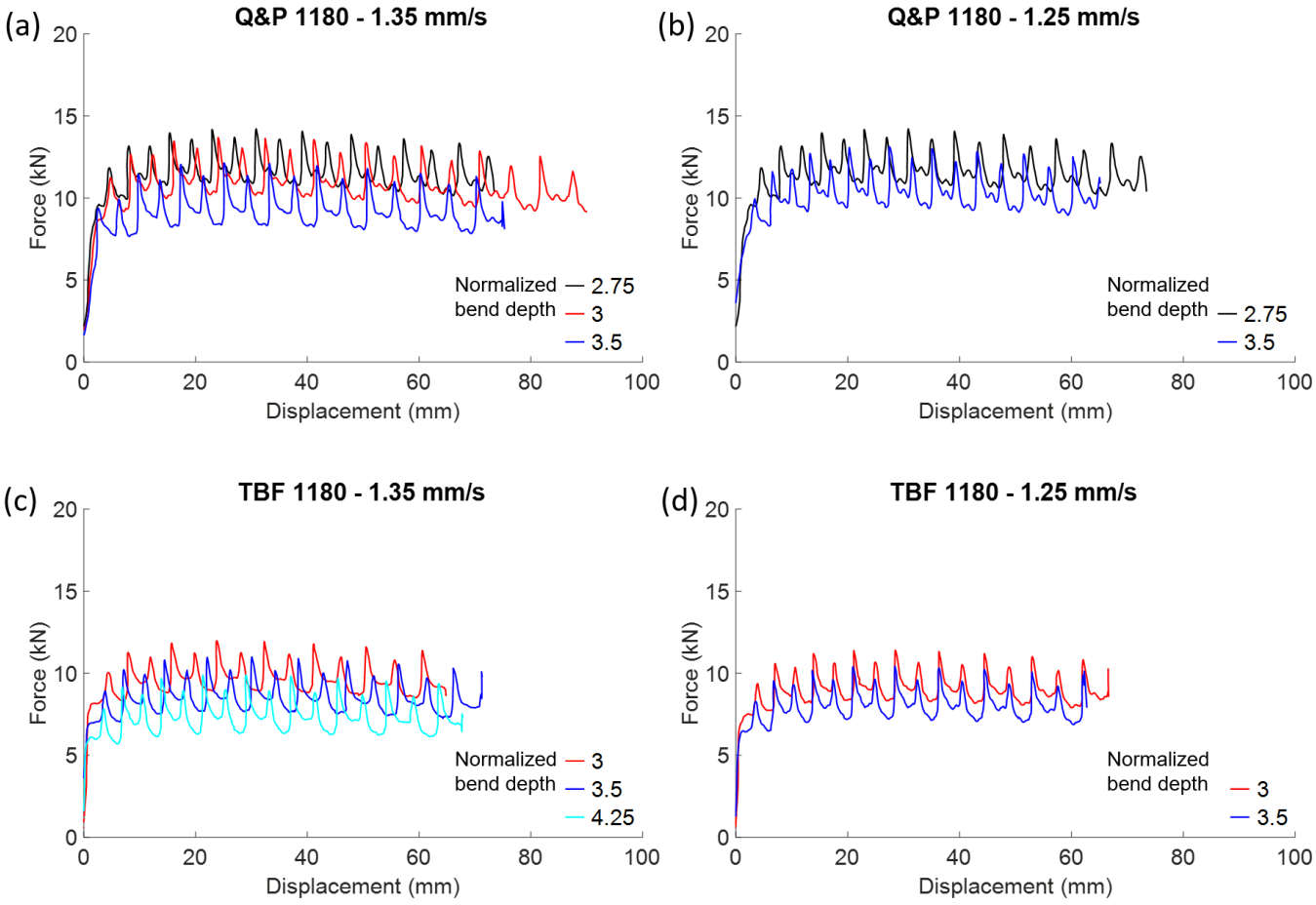


*Figure 5 Force-displacement curves for CBT for varying crosshead velocity and normalized bending depth. Q&P 1180 CBT curve comparison for a) 1.35 mm/s and b) 1.25mm/s crosshead velocity. TBF 1180 CBT curve comparison for c) 1.35 mm/s and d) 1.25 mm/s crosshead velocity.*

*Table 2 ETF values from the force-displacement curves for CBT in Figure 5 for 66mm/s carriage speed, varying crosshead velocity, and normalized bending depth (from Figure 5), along with the ratio of ETF for the 3x zone compared with ST.*

| Material | Sheet thickness (mm) | Crosshead velocity (mm/s) | Normalized bending depth | Engineering Strain (percent) | Improved ETF over ST |
|---|---|---|---|---|---|
| **Q&P 1180** | 1.2 | - | - | 10.5 (ST) | - |
| | | 1.35 | 2.75 | 39.63 | 3.77 |

| | | | | | |
|---|---|---|---|---|---|
| | | 1.35 | 3 | 47.9 | 4.56 |
| | | 1.35 | 3.5 | 40.04 | 3.81 |
| | | 1.25 | 2.75 | 39.04 | 3.71 |
| | | 1.25 | 3.5 | 34.64 | 3.29 |
| **TBF 1180** | 1 | - | - | 10.2 (ST) | - |
| | | 1.35 | 3 | 34.47 | 3.38 |
| | | 1.35 | 3.5 | 37.9 | 3.7 |
| | | 1.35 | 4.25 | 36.06 | 3.53 |
| | | 1.25 | 3 | 35.42 | 3.47 |
| | | 1.25 | 3.5 | 33.72 | 3.3 |

As mentioned earlier (see Figure 1), different regions of the gauge length undergo different levels of strain for the CBT specimens. Hence, the displacement and force values shown in Figure 5 cannot be compared directly with those resulting from ST. A more suitable comparison results from comparing the strain in only the 3x region of the CBT specimens with that of the ST specimens. The average strain of the 3x zone was extracted from the interrupted specimens via the DIC results for display in Figure 6. The median force in the given cycle preceding the interrupted point was determined as the basis for the load values shown in Figure 6. As shown in Figure 6a the 1.2 mm thick Q&P sheet produced 47.9% average elongation in the 3x zone under CBT in contrast to 10.5% elongation under ST, or a 4.6x improvement in ETF over ST. Similarly, results in Figure 6b show that the 1 mm thick TBF sheet produced a total of 37.9% elongation under CBT in contrast to 10.2% mm elongation under ST, which is equivalent to a 3.7x improvement in ETF over ST.

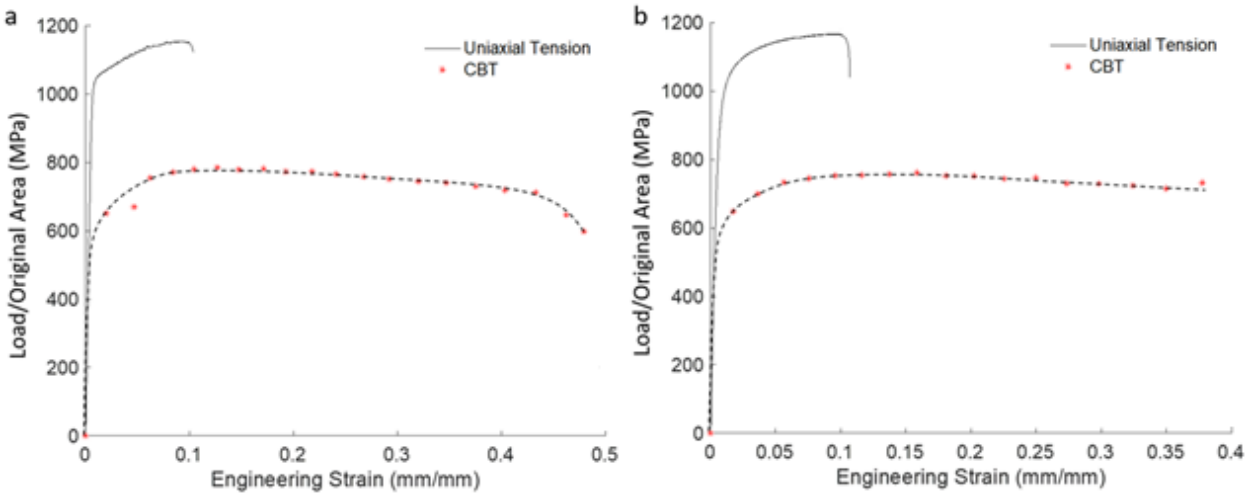


*Figure 6 Load/Original Area vs strain comparison for CBT and ST. The load/area corresponds to engineering stress for ST, but not for CBT which has a more complex stress state. The CBT values are measured in the 3x region at interrupted points of the process, taking the averaged load during the previous cycle. A): Q&P 1180, with CBT results for υ=1.35 mm/s and δ/t =3. B): TBF 1180, with CBT results for υ=1.35 mm/s and δ/t=3.5.*

For each of the CBT tests reported in this manuscript, failure occurred at the high-stress concentration resulting from the discontinuity in processing conditions at the 2x/3x interface. This is illustrated on the DIC-based strain map of the Q&P sheet, taken after 12 CBT cycles in Figure

7 (the 'ramp zones' are deliberated later in the Discussion section). The final average thickness of 1x, 2x, and 3x region is 1.03 mm, 0.94 mm, and 0.86 mm, respectively, highlighting the process-induced discontinuity between regions over which the rollers pass a different number of times. Figure 7 shows the final strain values at the 2x/3x interface being as high as 56.7%, in comparison to a strain of 49.5% in the center of the 3x region for Q&P. A comparison of strain development in the center of the 3x region, and at the 2x/3x interface region of the Q&P specimen, is shown in Figure 8. A similar DIC analysis of the ST specimen indicated that the surface strains peaked at ~29.7% in the necked region, compared with a global true strain of 10.5%.

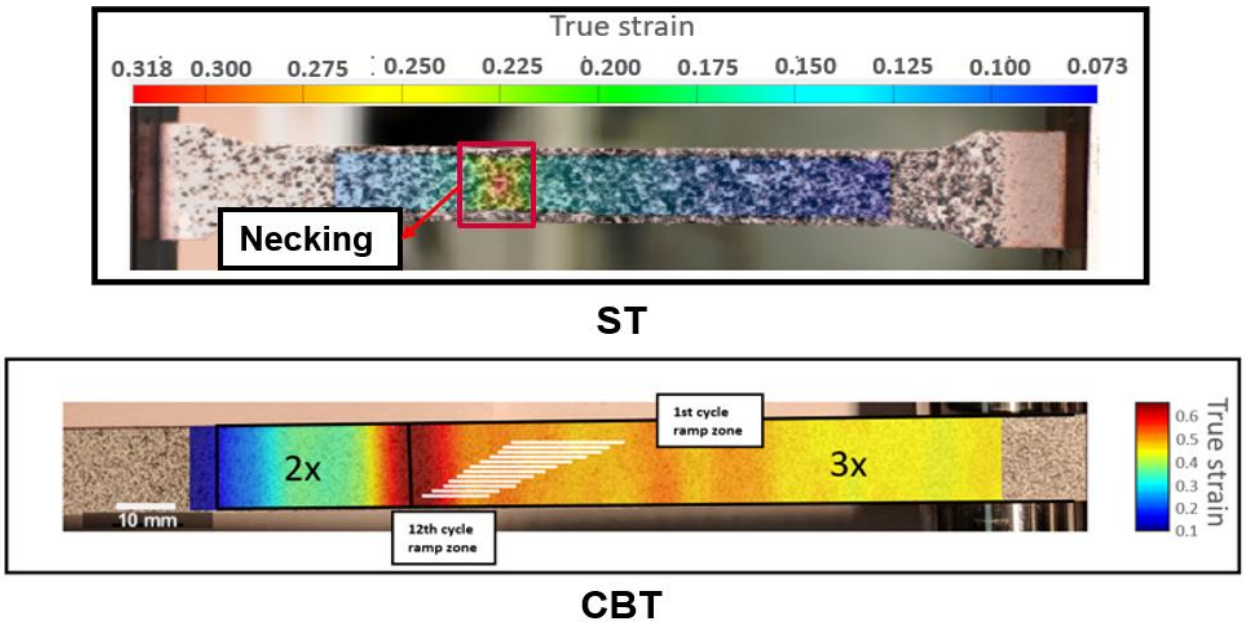


*Figure 7 Ncorr DIC image analysis result for Q&P 1180 just before fracture. The acceleration zone per cycle is highlighted by white bars. White represents the ramp-up zone position and size for each cycle with respect to the final cycle (just before failure). Results presented here are of Q&P 1180 but were similarly to those of the TBF 1180.*

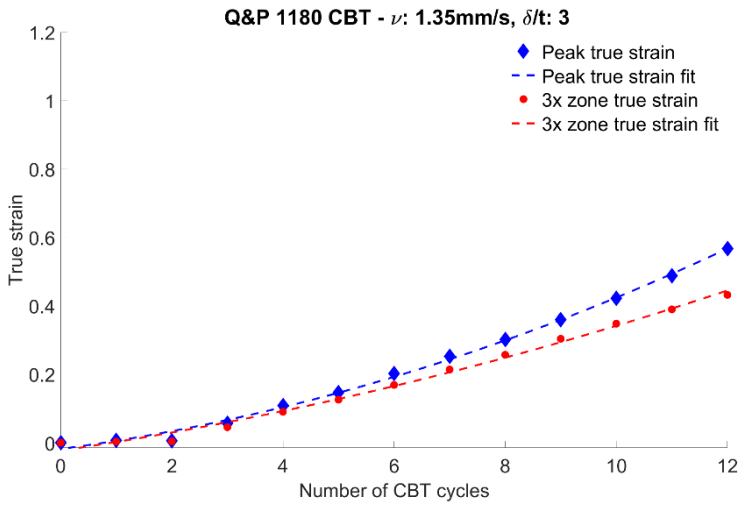


*Figure 8 Comparison between the accumulation of plastic strain at the 2x/3x strain zone interface (peak true strain) and 3x strain zone for the Q&P 1180 steel.*

Figure 9 compares the development of GND in the gauge length (away from the necking region) of ST and the high strain (3x) regions of CBT samples for both steels. The GND measurement presented in Figure 9 is near the surface of the samples; an analysis of GND variations across the CBT sample is discussed further below. The GND accumulation generally followed a linear trend with strain for both the deformation processes.

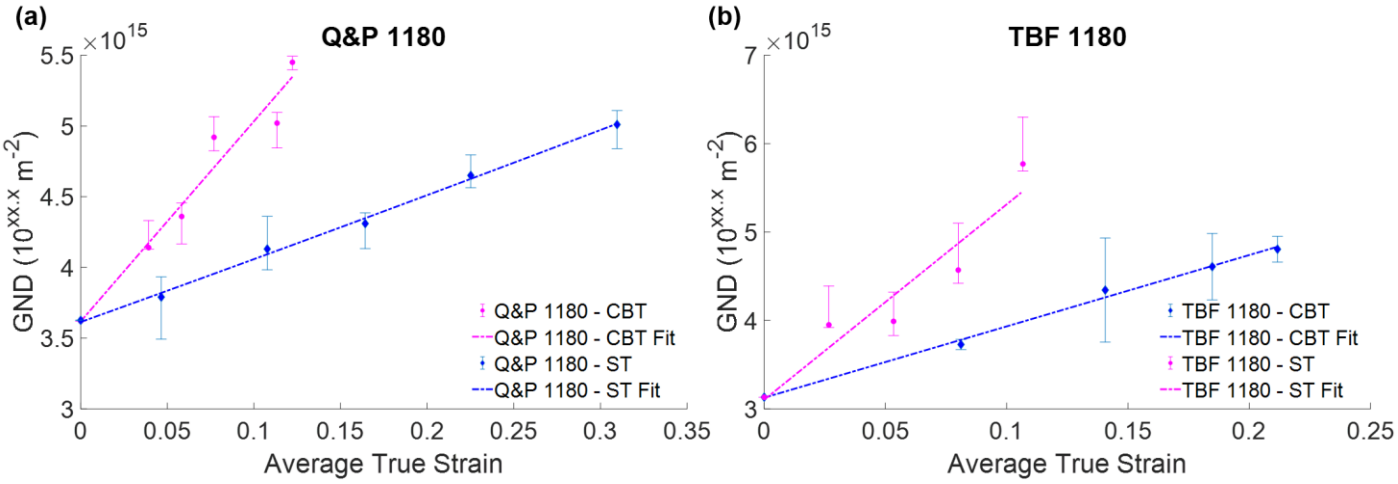


*Figure 9 Comparison of GND evolution between ST and CBT testing. a) Q&P 1180 and b) TBF 1180. The ST measurements were made away from the necked region but within the gauge section. The final GND measurements for CBT correspond to the 10th interrupted cycle for Q&P and the 8th interrupted cycle for TBF. The Q&P failed after the 12th CBT cycle and TBF failed after the 10th CBT cycle.*

*Table 3 GND values for several points across the thickness of the Q&P 1180 sample after CBT to failure. The sheet is nominally 1.2 mm thick.*

| Scan No. | Distance from the top edge (microns) | GND ($m^{-2}$) |
|---|---|---|
| 1 | 58 | 4.8977e+15 |
| 2 | 128 | 4.4074e+15 |
| 3 | 507 | 6.2357e+15 |
| 4 | 570 | 7.4905e+15 |
| 5 | 1038 | 4.7892e+15 |

In order to determine the profile of GND density across the sheet thickness, GND measurements were also taken from three regions of the Q&P steel – the two bending zones near the surfaces of the sheet, and the pure tension region in the middle (Table 3). As can be seen from the table, the GND in the monotonic tension zone of the sample (scans 3 and 4 in the middle of the sheet) is higher in comparison to the ratcheting zones (Scans 1, 2, and 5 near the edges).

Further insight into the CBT behavior was obtained by tracking the RA transformation rate. The RA fraction in this study was measured for three different areas for each strain level. It was

observed that the EBSD patterns deteriorated with increasing strain levels, therefore, a consistent clean-up method was employed across all scan data to remove incorrectly indexed or low confidence index (CI) patterns. The scan points with patterns having CI lower than 0.05 were removed and RA fraction was measured from the remaining points (Figure 10), consistent with the method developed in (Cramer et al., 2018). Previous studies found that the retained austenite (RA) measurements by EBSD are not as accurate as those of the XRD technique measurements. Kniff et al. (De Knijf et al., 2014) and Tirumalasetty et al. (Tirumalasetty et al., 2012a) attributed this effect to the limited spatial resolution of EBSD. However, Cramer et al. (Cramer et al., 2018) reported that for similar test conditions to those used here, the RA measurements by EBSD were within 3% of XRD measurements.

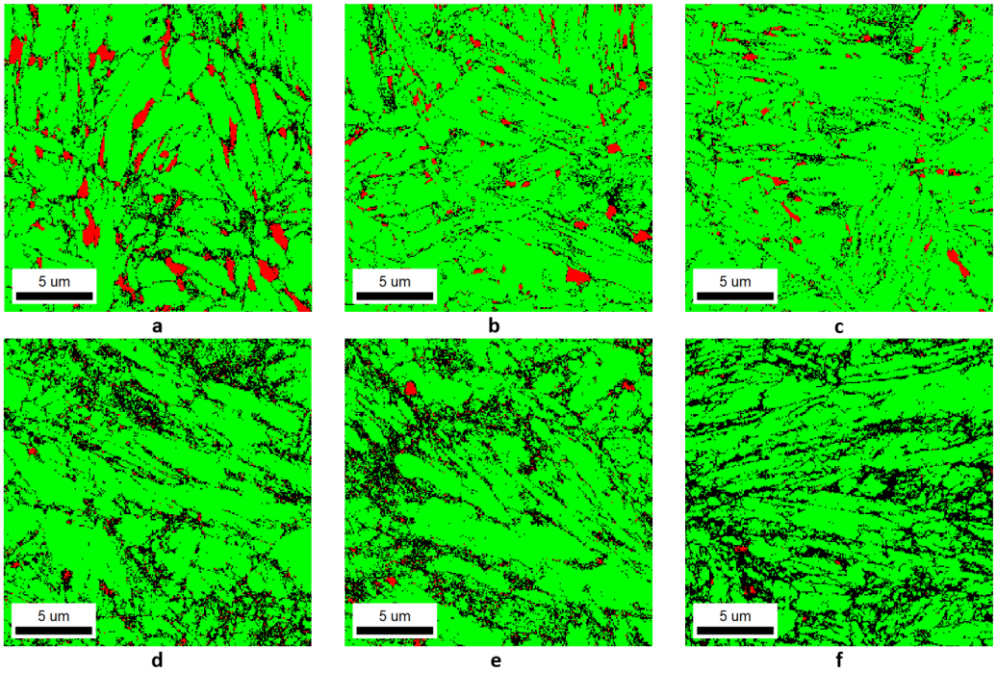


*Figure 10 The evolution of RA as a function of strain in CBT 3x strain zone samples for Q&P 1180 where RA is denoted by the color red, other phases (martensite and ferrite) by green, and points with CI less than 0.05 by black. a) 0% true strain/unstrained sample, b) 5.7%, c) 14.8%, d) 23.4%, e) 30.6% and f) 39.0% true strain.*

The EBSD-based measurement of RA in the two materials, for both CBT and ST, is shown in Figure 11 as a function of the fraction of elongation-to-failure (the CBT results are taken from the 3x region; the ST values are measured a significant distance away from the necked region). The decay in RA fraction follows an exponential curve for all cases, and the graphs highlight the similarity in transformation rate as a function of the fraction of failure strain. Since the failure strain of CBT-processed samples is much higher than ST, the deformation mode causes a slower transformation of RA, in comparison to ST.

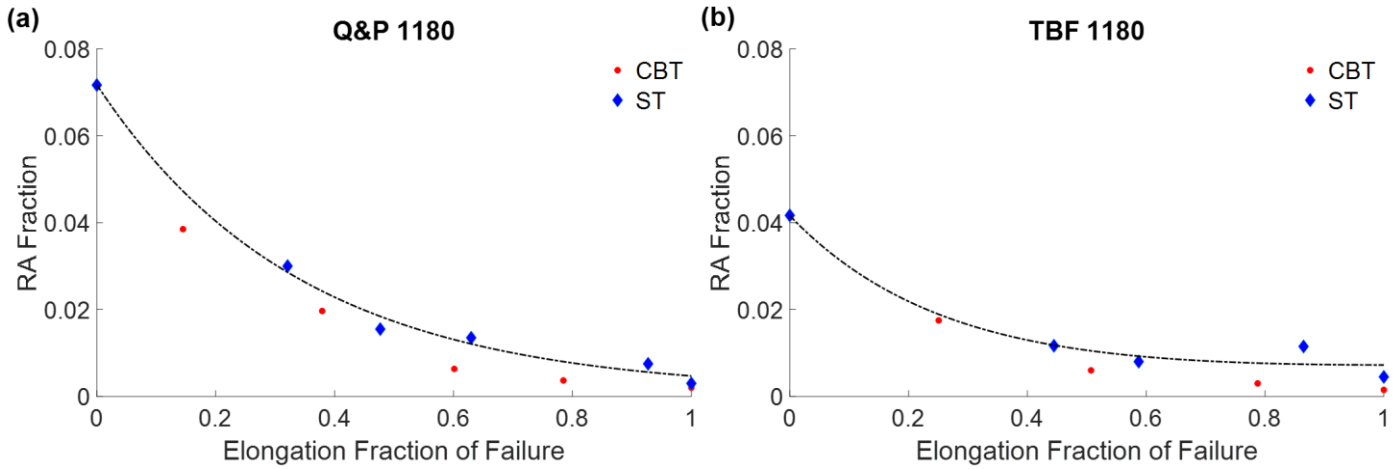


*Figure 11 RA evolution with respect to CBT and ST fraction of final ETF. The ST measurements were made away from the necked region but within the gauge section; the CBT measurements are made in the center of the 3x region.*

Table 4 compares RA transformation levels against actual strain values for a different view of the same data. ST deformation of Q&P 1180 resulted in a 50% transformation of RA at 0.032 average true strain. Under CBT forming, the same amount of RA transformation was achieved at a much higher average true strain of 0.06. Similar trends were observed for TBF.

*Table 4 Comparison between the average true strains achieved under ST vs CBT with respect to the RA transformation.*

| Percent of original RA | ST average true strain | CBT average true strain |
|---|---|---|
| 75% | 0.013 | 0.024 |
| 50% | 0.032 | 0.060 |
| 25% | 0.064 | 0.12 |

Finally, the amount of residual ductility in the CBT specimens at various strain levels was assessed, tensile specimens were waterjet cut from the 3x strain zone of the interrupted-CBT specimens and pulled under uniaxial tensile loading (ST). The test conditions for tensile specimens were similar to the ST tests mentioned in the previous section. As expected (Poulin et al., 2019), the strength of both steels increases and residual ductility decreases, with an increase in elongation/number of cycles in the CBT specimens. Figure 12 compares the residual ductility (normalized by the elongation value of the ST specimens) in the interrupted CBT specimens and ST specimens (y-axis), as a fraction of failure strain of uninterrupted CBT tests (x-axis). If the ST ductility decreased at the same relative rate as the CBT ductility, then one would expect that after the CBT specimen had been stretched to 50% of failure, then, when pulled in ST, it would stretch to 50% of the ST elongation; the experimental data points would thus lie along the solid line in Figure 12. However, it can be seen that the post-CBT ST ductility is exhausted much more rapidly than the CBT ductility; after being elongated to only 10% of CBT failure strain, for example, the Q&P steel has already exhausted nearly 70% of its ST ductility. Also, unlike ST deformation from the base material, interrupted CBT specimens that underwent subsequent ST testing demonstrated a rapid loss in ductility.

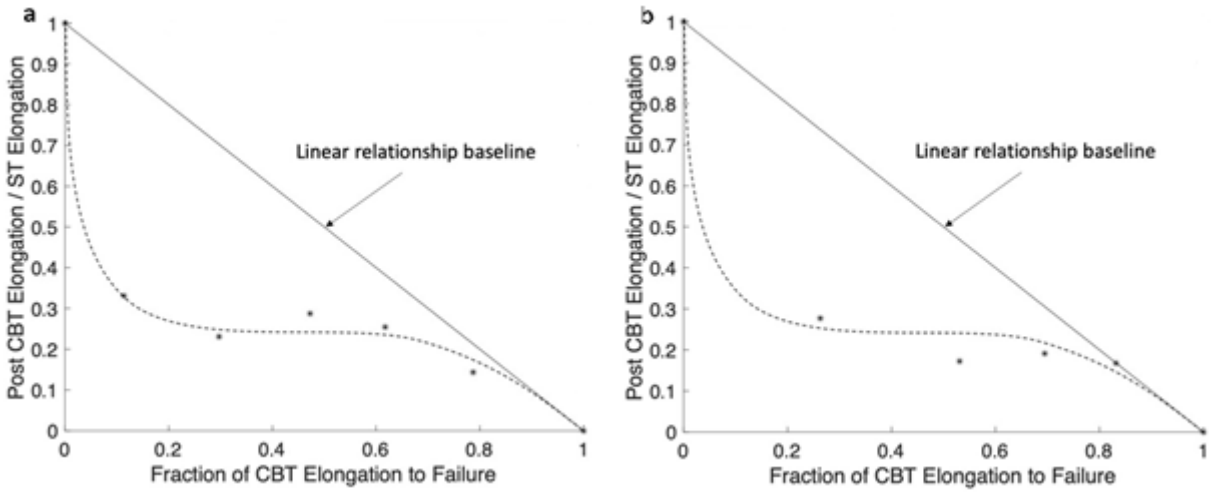


*Figure 12 Elongation of interrupted CBT specimens as a fraction of final elongation (x-axis) and subsequent elongation under ST of these specimens, as a fraction of ST elongation of an unprocessed specimen (y-axis). The residual ductility measurements of interrupted CBT specimens in comparison to the ST elongation, as a fraction of fracture. The ideal comparison is indicated by the solid line. A trendline is fitted to the Q&P data (left), and the same trendline is shown for the TBF specimen (right), in order to aid in the comparison.*

Insights into the different failure modes can be gained from Figure 13, which shows typical edge-on views of the failed sheets for the three types of tests (ST, CBT, and CBT-followed-by-ST).

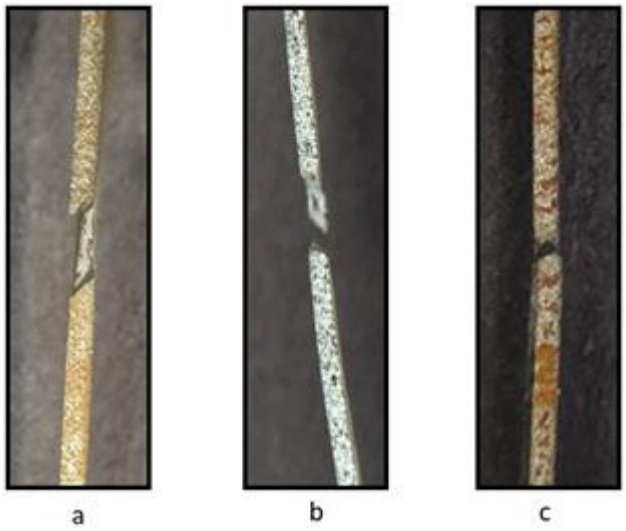


*Figure 13 Fracture edge of Q&P 1180 failed under a) pure-ST, b) pure-CBT and c) residual ductility test (2-cycles interrupted CBT specimen, failed under ST). The same trends were observed for TBF 1180.*

## Discussion

Initial insights are gained from the CBT tests with varying parameter values. While the number of data points is limited (in terms of crosshead velocity (υ) and roller depth), the force-displacement curves (Figure 5) reveal the inverse relationship between the measured pulling force

on the sheet and the normalized bending depth, δ/t, for a fixed υ. As the roller depth increases, the amount of bending also rises, leading to a lower net tensile force required to cause plastic deformation. In contrast, increasing υ for fixed δ/t and carriage velocity increases the amount of sheet that experiences plastic strain due to tension which reduces ETF. In fact, the sheet can approach pure tensile state when υ is higher than a certain limit for a constant carriage velocity. Consequently, the majority of the sheet will deform under tension rather than incremental bending. The study by Emmens et al. (Emmens and van den Boogaard, 2009a) observed the same relationship between ETF, υ, and δ/t for a fixed carriage velocity. However, no increase in tensile force was observed because of only a 0.1 mm/s increment in the υ. In our experiments, a value of υ = 1.35 mm/s yielded more elongation for the corresponding optimum values of δ/t than a value of 1.25 mm/s, as shown in Figure 5 and Table 2. This is in-line with results from the previous detailed parametric study (Poulin et al., 2019).

Figure 6 highlights the difference between CBT and ST in terms of tensile loads vs engineering strain (3x region for the CBT specimens). A combination of a slower rate of strain hardening and RA transformation, and delayed localization facilitates higher ETF in the CBT specimens. The lower tensile loads for CBT forming are a direct response to superimposing bending-on-tension. This is an indication of lower strain hardening in CBT, it is better reflected in the GND comparison as shown in Figure 9 where CBT demonstrates a more gradual GND development than ST. A slower RA transformation rate under CBT (Figure 11) further adds to the overall increase in ductility of both the alloys and helps delay localization.

As mentioned earlier, the bending depth was normalized following the Poulin et. al. study (Poulin et al., 2019) where the total applied bending in the sheet was divided by the thickness of the unstrained specimen, i.e., δ/t. The experiments conducted for the current study revealed that normalizing the bending depth for both steels did not result in a consistent optimal value for both steels. In fact, the unnormalized values of bend depth (3.6 mm for Q&P and 3.5 mm for TBF) are closer together than the normalized values. It could be that the normalization is not appropriate, or that the difference in the behavior of the two steels is too great. In summary, the Q&P steel shows greater ductility improvement under CBT compared with the TBF steel, possibly from the slightly greater thickness of the sheet, as well as the difference in the microstructure of the two steels (including ~2% higher RA in Q&P 1180).

One interesting observation highlighted by the DIC strain map (Figure 7) is the formation of strain undulations in the 3x strain zone. The effect may be partly attributed to the change in deformation associated with the ramp-up and down in the carriage speed as it leaves and approaches either end of the CBT apparatus. As the carriage gets closer to the end of a stroke, it decelerates to avoid activating the safety kill-switch. The crosshead keeps moving at a constant rate while the carriage is slowing down and accelerating in the other direction. This causes uneven strain development in this acceleration region of the specimen. Figure 7 also shows the acceleration zones for each cycle (shown as white lines), with those from early cycles moving to the right as the specimen stretches. It can be seen from the DIC strain map that the undulations extend beyond the acceleration zone, indicating that some deformation instability reaches further into the 3x region. Eliminating these irregularities (regions crossed by differing numbers of rollers, and

acceleration zones) from the current CBT forming apparatus could significantly improve the resultant elongation in the sheet.

The more severe strain heterogeneity at the interfaces between regions that see different numbers of roller passes results in failure of all CBT samples at the 2x/3x interface (Figure 7). The final strain in the regions of failure was significantly higher than the main 3x section, indicates that the failure strain in the fully processed 3x region would likely be at least the same value. For Q&P 1180 the maximum strain at the 2x/3x interface was 56.7% - an increase of 15% over the maximum measured values in the 3x region. In the ST test on the same steel, the maximum strain in the necked region was 29.7%. The implication is that by purely delaying necking, the strain to failure of Q&P steel under ST could be increased from 10.5% to almost 30%. However, CBT can increase the elongation to ~57%. Hence the delayed necking aspect of the CBT approach accounts for only about half of the improvement in elongation. Some other mechanism appears to be contributing to the increased elongation for CBT samples.

The discussion of delayed necking is aided by the observations of GND evolution in the various samples. Under a typical ST deformation, soft regions of a steel will deform first, thus generating dislocations in the area, leading to local hardening. During subsequent straining, a different region of soft material will harden. This incremental hardening continues until ductility is exhausted, and strain localization occurs, leading to necking and failure (Hutchinson, 1964). CBT deformation differs in at least two significant ways. Firstly, at any given time the deformation does not occur uniformly along the gauge length but is localized to the regions passing over rollers. The region being deformed moves up and down the gauge length with the rollers, discouraging a strain localization in a single area. Secondly, CBT involves a through-thickness strain gradient in the bent region of the sheet as it passes over the roller. The central zone of the sheet experiences monotonic tension till fracture while the outer zones experience ratcheting due to bending-unbending nature of the deformation (Emmens and van den Boogaard, 2011). Simulations in a similar study of 1.4 mm thick DP780 sheet by Barrett et al. revealed that the stress state in the sheet plane is globally tensile; the applied tensile stress is larger than the locally superimposed bending stresses, hence the dominant contributor to effective strain in the sheet is along the tensile direction at every point (Barrett and Knezevic, 2020). Nevertheless, the ratcheting behavior near the sheet surfaces potentially leads to different dislocation structure formation, compared with ST deformation. A recent study showed that, while dislocation structures forming in grains during ST appear disorganized, cellular substructures are observed to form in CBT processing of alloy AA6022-T4 (Knezevic et al., 2019). Such cellular substructures evolve from loose tangles of dislocations to well-defined walls with increasing CBT cycles. The observations were made by transmission electron microscopy. These dislocation patterns influence the hardening behavior of the sample. In the current study, HREBSD is used to extract GND density at various points in the deformation process, as a proxy for the total dislocation density (relating to the total hardening that has occurred).

Figure 9 shows a more gradual increase in the GND values for the near-surface regions of the CBT sample for both steels, in comparison to ST. This indicates a lower strain hardening rate in the CBT process (by around a factor of 4), potentially contributing to the higher elongation. The

GND values for CBT samples are not available all the way to failure, however, the general trend indicates a generally linear relationship between GND density and fraction of ETF for both ST and CBT, i.e., rate of GND accumulation correlates with elongation to failure, and hence is likely a causal factor in the delayed failure of CBT samples.

Furthermore, Table 3 indicates that there is a significant difference between GND content in the middle of the CBT sheets compared with near the surface of the sheet. In fact, the GND content near the center of the CBT sheet is closer to the GND content in the ST samples, at the same strain levels. This indicates that the cyclical bending/unbending that occurs near the surface of the sheet results in slower GND accumulation compared to the center of the sheet, which experiences only tensile strain. The contrast between damage accumulation in the center of the sheet compared with the surface regions is also highlighted by the residual ductility data. Figure 12 demonstrates remarkably low residual ductility in CBT samples, after only low levels of CBT processing. If the CBT hardening/dislocation accumulation rate is lower than ST, then one would expect higher residual ductility. However, the fracture surfaces of the residual ductility samples may help to explain the conundrum. The fracture profile for the CBT-followed-by-ST specimen is completely different from the CBT-only and ST-only specimens (Figure 13). The former displays a cup and cone profile, compared to a flat fracture surface in pure ST and CBT specimens. This indicates a significant amount of damage accumulation in the center (tensile) section of the sheet during CBT. Stress triaxiality is the greatest in this center region, also contributing to damage evolution (Li et al., 2020). When the sheet is put into tension after interrupting the CBT process, the void coalescence produces the cup and cone fracture surface. This leads to the low levels of residual ductility reported in Figure 12.

We now consider the evolution of RA in the two steels during deformation. It is generally assumed that RA transformation is most effective at increasing ductility for a forming operation when it happens at a uniform rate over the entire strain range (Fischer et al., 2000; Ma and Hartmaier, 2015). However, it has been observed in previous publications that ST is associated with rapid initial RA transformation, rather than the desired uniform rate for Q&P and TBF 1180 (Cramer et al., 2018; Gibbs, 2019). Other studies have considered various strain paths. Experiments performed with hole expansion (Yoon et al., 2016), draw bend fracture (DBF) and wide draw bend fracture (WDBF) (Li et al., 2016), and limiting dome height (LDH) tests (Bhargava et al., 2015) have reported an increase in ETF over ST in TRIP steels, owing to more effective RA transformation. A study by Cramer et al. on the deformation behavior of Q&P 1180 steel using LDH tests found an inverse correlation between the initial RA transformation rate and the failure strain for a given strain path; the highest effective strain levels were achieved under biaxial tension followed by plane-strain, and then uniaxial tension (Cramer et al., 2018). The relationships between strain path and RA transformation rates have also been confirmed theoretically using crystal plasticity theory (Cluff et al., 2021; Feng et al., 2021a; Feng et al., 2021b; Zecevic et al., 2019).

The strain path during CBT involves a combination of tension and bending where a significant amount of the plastic deformation in the sheet relates to bending. Sheet forming via bending has been found to cause higher stress triaxiality than uniaxial tension (Talebi-Ghadikolaee et al., 2020).

Young, in their study on the stress state dependency of the TRIP mechanism in two metastable austenitic steels postulated that RA transformation rate increase with increasing stress triaxiality (Young, 1988). However, Figure 11 and Table 4 indicate a much slower transformation rate in CBT compared to ST when plotted against effective strain; when plotted against the fraction of ETF, the transformation rates are remarkably similar. The studies by Polatidis et al. and Beese et al. have shown that RA transformation is not a monotonic function of stress triaxiality (Beese and Mohr, 2011; Polatidis et al., 2021). Polatidis et al. further concluded that the number of martensite nucleation sites has a stronger effect on RA transformation rather than stress triaxiality. Hence there is no simple relationship between RA transformation rate and strain path that would explain the slower RA transformation rate with effective strain in the CBT case. A more detailed study of the complex deformation process during CBT and the RA transformation is required. As for the rate of GND accumulation, the RA transformation rate correlates well with ETF for ST and CBT, indicating that it too is a significant factor in the extended elongation induced by CBT. Furthermore, RA transformation influences the hardening rate (Chiang et al., 2011; POLAT et al., 2012; Wei et al., 2007; Yu et al., 2006), potentially also affecting the GND accumulation rate and resulting final exhaustion of ductility.

## Conclusions

Incremental sheet forming via CBT was found to dramatically increase elongation to fracture in two TRIP-assisted steels, Q&P 1180 and TBF 1180. The following conclusions were drawn from the experimental results, which included DIC and HR-EBSD observations:

1. Optimal parameters result in ETF of 4.6x and 3.7x higher than ST for Q&P and TBF, respectively. If the specimens had not failed at the strain discontinuity caused by the process set up, the ETF would likely be at least 15% higher.
2. Continually changing the volume being deformed during CBT helps to delay necking; however, a comparison between localized strain in the necked region of an ST sample and the failure region of a CBT sample indicates that this mechanism could only account for about half of the increased ETF.
3. Near-surface GND density in the CBT samples increased linearly with strain in both ST and CBT samples, with the ST GND content increasing at about 4 times the rate of the CBT samples. The slower accumulation of dislocations measured in the CBT samples correlates with the higher ETF observed during testing.
4. The GND accumulation in the center of the CBT-processed sheets, where there was negligible bending / unbending strain component, was twice that the surface. This appears to contribute to the low residual ductility in partially processed CBT samples that are subsequently pulled in ST. This observation is also supported by the fracture surface of these samples, indicating higher accumulated damage in the sheet center.
5. The RA transformation in the CBT specimens follows a similar curve to that of the ST specimens when plotted as a function of the fraction of ETF. Hence, as for GND

accumulation rate, a lower RA transformation rate during CBT correlates with higher ETF, indicating that the slower transformation rate is a strong contributor to higher ductility during CBT.

**Acknowledgments**

The BYU team was funded by the National Science Foundation (NSF) under grant CMMI 1926662, and DMR 1507095. C.M.P. and M.K. would like to acknowledge the support provided by the NSF under grant OIA-1757371.

**Data Availability**

The raw/processed data required to reproduce these findings cannot be shared at this time due to technical or time limitations.

**References**

2010. OIM 6.0. EDAX-TSL.
2014. Matlab R2014b, 7.3 ed. The Mathworks, Inc.
Ahmed, N., Hartmaier, A., 2010. A two-dimensional dislocation dynamics model of the plastic deformation of polycrystalline metals. Journal of the Mechanics and Physics of Solids 58, 2054-2064.
Antolovich, S.D., Armstrong, R.W., 2014. Plastic strain localization in metals: origins and consequences. Progress in Materials Science 59, 1-160.
Barrett, T.J., Knezevic, M., 2020. Modeling material behavior during continuous bending under tension for inferring the post-necking strain hardening response of ductile sheet metals: Application to DP 780 steel. International Journal of Mechanical Sciences 174, 105508.
Barrett, T.J., Takagi, S., Islam, N., Kuwabara, T., Hassan, T., Kinsey, B.L., Knezevic, M., Korkolis, Y.P., 2020. Material modeling and simulation of continuous-bending-under-tension of AA6022-T4. Journal of Materials Processing Technology, 116658.
Beese, A.M., Mohr, D., 2011. Effect of stress triaxiality and Lode angle on the kinetics of strain-induced austenite-to-martensite transformation. Acta Materialia 59, 2589-2600.
Bhargava, M., Chakrabarty, S., Barnwal, V.K., Tewari, A., Mishra, S.K., 2018. Effect of microstructure evolution during plastic deformation on the formability of Transformation Induced Plasticity and Quenched & Partitioned AHSS. Materials & Design 152, 65-77.
Bhargava, M., Tewari, A., Mishra, S.K., 2015. Forming limit diagram of Advanced High Strength Steels (AHSS) based on strain-path diagram. Materials and Design 85, 149-155.
Billur, E., Altan, T., 2013. Three generations of advanced high-strength steels for automotive applications, Part I. Stamp. J, 16-17.
Blaber, J., 2014. Ncorr digital image correlation software. Georgia Institute of Technology.
Blaber, J., Adair, B., Antoniou, A., 2015. Ncorr: open-source 2D digital image correlation matlab software. Exp. Mech. 55, 1105-1122.
BYU, 2015. OpenXY, 1.0 ed. github.com.

Cantara, A.M., Zecevic, M., Eghtesad, A., Poulin, C.M., Knezevic, M., 2019. Predicting elastic anisotropy of dual-phase steels based on crystal mechanics and microstructure. International Journal of Mechanical Sciences 151, 639-649.
Chiang, J., Lawrence, B., Boyd, J.D., Pilkey, A.K., 2011. Effect of microstructure on retained austenite stability and work hardening of TRIP steels. Materials Science and Engineering: A 528, 4516-4521.
Cluff, S., Knezevic, M., Miles, M.P., Fullwood, D.T., Mishra, R.K., Sachdev, A.K., Brown, T., Homer, E.R., 2021. Coupling kinetic Monte Carlo and finite element methods to model the strain path sensitivity of the isothermal stress-assisted martensite nucleation in TRIP-assisted steels. Mechanics of Materials 154, 103707.
Cramer, J., Adams, D., Miles, M.P., Fullwood, D.T., Homer, E.R., Brown, T., Mishra, R.K., Sachdev, A., 2018. Effect of strain path on forming limits and retained austenite transformation in Q&P 1180 steel. Materials Science and Engineering: A 734, 192-199.
De Knijf, D., Petrov, R., Föjer, C., Kestens, L.A., 2014. Effect of fresh martensite on the stability of retained austenite in quenching and partitioning steel. Materials Science and Engineering: A 615, 107-115.
Eghtesad, A., Knezevic, M., 2020. High-performance full-field crystal plasticity with dislocation-based hardening and slip system back-stress laws: Application to modeling deformation of dual-phase steels. J. Mech. Phys. Solids 134, 103750.
Emmens, W.C., van den Boogaard, A.H., 2009a. Incremental forming by continuous bending under tension-An experimental investigation. Journal of Materials Processing Technology 209, 5456-5463.
Emmens, W.C., van den Boogaard, A.H., 2009b. Incremental forming by continuous bending under tension—An experimental investigation. Journal of Materials Processing Technology 209, 5456-5463.
Emmens, W.C., van den Boogaard, A.H., 2009c. An overview of stabilizing deformation mechanisms in incremental sheet forming. Journal of Materials Processing Technology 209, 3688-3695.
Emmens, W.C., van den Boogaard, A.H., 2011. Cyclic stretch-bending: Mechanics, stability and formability. Journal of Materials Processing Technology 211, 1965-1981.
Feng, Z., Mamros, E.M., Ha, J., Kinsey, B.L., Knezevic, M., 2021a. Modeling of plasticity-induced martensitic transformation to achieve hierarchical, heterogeneous, and tailored microstructures in stainless steels. CIRP Journal of Manufacturing Science and Technology 33, 389-397.
Feng, Z., Zecevic, M., Knezevic, M., 2021b. Stress-assisted ($\gamma \rightarrow \alpha'$) and strain-induced ($\gamma \rightarrow \varepsilon \rightarrow \alpha'$) phase transformation kinetics laws implemented in a crystal plasticity model for predicting strain path sensitive deformation of austenitic steels. International Journal of Plasticity 136, 102807.
Fischer, F.D., Reisner, G., Werner, E., Tanaka, K., Cailletaud, G., Antretter, T., 2000. A new view on transformation induced plasticity (TRIP). International Journal of Plasticity 16, 723-748.
Gibbs, P.K., 2019. Strain Path Effect on Austenite Transformation and Ductility in TBF 1180 Steel.
Harilal, R., 2014. Adaptation of open source 2D DIC software Ncorr for solid mechanics applications.
Hirsch, J., Al-Samman, T., 2013. Superior light metals by texture engineering: Optimized aluminum and magnesium alloys for automotive applications. Acta. Mater. 61, 818-843.

Hutchinson, J., 1964. Plastic stress-strain relations of FCC polycrystalline metals hardening according to Taylor's rule. Journal of the Mechanics and Physics of Solids 12, 11-24.
Knezevic, M., Poulin, C.M., Zheng, X., Zheng, S., Beyerlein, I.J., 2019. Strengthening of alloy AA6022-T4 by continuous bending under tension. Mater. Sci. Eng. A 758, 47-55.
Li, D., Chen, Z., Sun, L., Lee, J., Wagoner, R., 2016. An improved test for shear fracture. International Journal of Solids and Structures 97, 29-42.
Li, Z., Kiran, R., Hu, J., Jr., L.G.H., Bower, A.F., 2020. Analysis and design of a three-phase TRIP steel microstructure for enhanced fracture resistance. Int J Fracture 221, 53-85.
Ma, A., Hartmaier, A., 2015. A study of deformation and phase transformation coupling for TRIP-assisted steels. Int. J. Plast. 64, 40-55.
Ma, B.L., Liu, Z.G., Jiang, Z., Wu, X.D., Diao, K.S., Wan, M., 2016. Prediction of forming limit in DP590 steel sheet forming: An extended fracture criterion. Materials & Design 96, 401-408.
Matlock, D.K., Speer, J.G., 2010. Processing Opportunities for New Advanced High-Strength Sheet Steels. Materials and Manufacturing Processes 25, 7-13.
Nikhare, C., Kinsey, B.L., Korkolis, Y., 2012. Numerical Investigation of Residual Formability and Deformation Localization during Continuous-Bending-under-Tension, ASME 2012 International Manufacturing Science and Engineering Conference collocated with the 40th North American Manufacturing Research Conference and in participation with the International Conference on Tribology Materials and Processing. American Society of Mechanical Engineers Digital Collection, pp. 139-144.
POLAT, A., ÖZTÜRK, F., TOROS, S., 2012. The effects of strain rate and temperature on the mechanical properties of TRIP800 steel, International Iron & Steel Symposium, Karabük, Türkiye, pp. 910-915.
Polatidis, E., Haidemenopoulos, G.N., Krizan, D., Aravas, N., Panzner, T., Šmíd, M., Papadioti, I., Casati, N., Van Petegem, S., Van Swygenhoven, H., 2021. The effect of stress triaxiality on the phase transformation in transformation induced plasticity steels: Experimental investigation and modelling the transformation kinetics. Materials Science and Engineering: A 800, 140321.
Poulin, C.M., Barrett, T.J., Knezevic, M., 2020. Inferring Post-Necking Strain Hardening Behavior of Sheets by a Combination of Continuous Bending Under Tension Testing and Finite Element Modeling. Experimental Mechanics 60, 459-473.
Poulin, C.M., Korkolis, Y.P., Kinsey, B.L., Knezevic, M., 2019. Over five-times improved elongation-to-fracture of dual-phase 1180 steel by continuous-bending-under-tension. Materials & Design 161, 95-105.
Roemer, T.J., Barrett, T.J., Knezevic, M., Kinsey, B.L., Korkolis, Y.P., 2019. Experimental study of continuous-bending-under-tension of AA6022-T4. Journal of Materials Processing Technology 266, 707-714.
Roemer, T.J., Kinsey, B.L., Korkolis, Y.P., 2015. Design of a continuous-bending-under-tension machine and initial experiments on AL-6022-T4, ASME 2015 International Manufacturing Science and Engineering Conference. American Society of Mechanical Engineers Digital Collection.
Ruggles, T., Fullwood, D., 2013. Estimations of Bulk Geometrically Necessary Dislocation Density Using High Resolution EBSD. Ultramicroscopy 133, 8-15.
Sanchez, L.R., 2010. Modeling of springback, strain rate and Bauschinger effects for two-dimensional steady state cyclic flow of sheet metal subjected to bending under tension. International Journal of Mechanical Sciences 52, 429-439.

Scalici, T., Fiore, V., Orlando, G., Valenza, A., 2015. A DIC-based study of flexural behaviour of roving/mat/roving pultruded composites. Composite Structures 131, 82-89.
Talebi-Ghadikolaee, H., Naeini, H.M., Mirnia, M.J., Mirzai, M.A., Gorji, H., Alexandrov, S., 2020. Fracture analysis on U-bending of AA6061 aluminum alloy sheet using phenomenological ductile fracture criteria. Thin-Walled Structures 148, 106566.
Tamura, I., 1982. Deformation-Induced Martensitic-Transformation and Transformation-Induced Plasticity in Steels. Metal Science 16, 245-253.
Tirumalasetty, G., Van Huis, M., Kwakernaak, C., Sietsma, J., Sloof, W., Zandbergen, H., 2012a. Deformation-induced austenite grain rotation and transformation in TRIP-assisted steel. Acta Materialia 60, 1311-1321.
Tirumalasetty, G.K., van Huis, M.A., Kwakernaak, C., Sietsma, J., Sloof, W.G., Zandbergen, H.W., 2012b. Deformation-induced austenite grain rotation and transformation in TRIP-assisted steel. Acta Materialia 60, 1311-1321.
Wei, X., Fu, R., Li, L., 2007. Tensile deformation behavior of cold-rolled TRIP-aided steels over large range of strain rates. Materials Science and Engineering: A 465, 260-266.
Weng, G., 1990. The overall elastoplastic stress-strain relations of dual-phase metals. Journal of the Mechanics and Physics of Solids 38, 419-441.
Yaddanapudi, K., Knezevic, M., Mahajan, S., Beyerlein, I.J., 2021. Plasticity and structure evolution of ferrite and martensite in DP 1180 during tension and cyclic bending under tension to large strains. Mater. Sci. Eng. A 820, 141536.
Yoon, J.I., Jung, J., Lee, H.H., Kim, G.-S., Kim, H.S., 2016. Factors governing hole expansion ratio of steel sheets with smooth sheared edge. Met Mater-Int 22, 1009-1014.
Yoshida, F., Hamasaki, H., Uemori, T., 2015. Modeling of anisotropic hardening of sheet metals including description of the Bauschinger effect. International Journal of Plasticity 75, 170-188.
Young, C.-C., 1988. Transformation toughening in phosphocarbide-strengthened austenitic steels. Massachusetts Institute of Technology.
Yu, H.Y., Kai, G.Y., De Jian, M., 2006. Transformation behavior of retained austenite under different deformation modes for low alloyed TRIP-assisted steels. Materials Science and Engineering: A 441, 331-335.
Zecevic, M., Beyerlein, I.J., Knezevic, M., 2017. Coupling elasto-plastic self-consistent crystal plasticity and implicit finite elements: Applications to compression, cyclic tension-compression, and bending to large strains. Int. J. Plast. 93, 187-211.
Zecevic, M., Korkolis, Y.P., Kuwabara, T., Knezevic, M., 2016a. Dual-phase steel sheets under cyclic tension–compression to large strains: Experiments and crystal plasticity modeling. J. Mech. Phys. Solids 96, 65-87.
Zecevic, M., Roemer, T., Knezevic, M., Korkolis, Y., Kinsey, B., 2016b. Residual Ductility and Microstructural Evolution in Continuous-Bending-under-Tension of AA-6022-T4. Materials 9, 130.
Zecevic, M., Upadhyay, M.V., Polatidis, E., Panzner, T., Van Swygenhoven, H., Knezevic, M., 2019. A crystallographic extension to the Olson-Cohen model for predicting strain path dependence of martensitic transformation. Acta. Mater. 166, 386-401.